

# Ultra-fast, high-power MUTC Photodiodes with bandwidth-efficiency product over 130 GHz × 100%

Linze Li,<sup>1,2,\*</sup> Tianyu Long,<sup>1,2,\*</sup> Xiongwei Yang,<sup>3,4,5,\*</sup> Zhouze Zhang,<sup>1</sup> Luyu Wang,<sup>1,2</sup>  
Jingyi Wang,<sup>1,2</sup> Mingxu Wang,<sup>3,4,5</sup> Juanjuan Lu,<sup>1</sup> Jianjun Yu,<sup>3,4,5,†</sup> and Baile Chen<sup>1,‡</sup>

<sup>1</sup>*School of Information Science and Technology, ShanghaiTech University, Shanghai 201210, China*

<sup>2</sup>*Fastphide Photonics, Shanghai 201210, China*

<sup>3</sup>*China State Key Laboratory of ASIC and System, Fudan University, Shanghai 200433, China*

<sup>4</sup>*Key Laboratory for Information Science of Electromagnetic Waves,*

*Shanghai Institute for Advanced Communication and Data Science, Fudan University, Shanghai 200433, China*

<sup>5</sup>*School of Information Science and Technology, Fudan University, Shanghai 200433, China*

**The accelerating demand for wireless communication necessitates wideband, energy-efficient photonic sub-terahertz (sub-THz) sources to enable ultra-fast data transfer. However, as critical components for THz photonic mixing, photodiodes (PDs) face a fundamental trade-off between quantum efficiency and bandwidth, presenting a major obstacle to achieving high-speed performance with high optoelectronic conversion efficiency. Here, we overcome this challenge by demonstrating an InP-based, waveguide-integrated modified uni-traveling carrier photodiode (MUTC-PD) with a terahertz bandwidth exceeding 200 GHz and a bandwidth-efficiency product (BEP) surpassing 130 GHz × 100%. Through the integration of a spot-size converter (SSC) to enhance external responsivity, alongside optimized electric field distribution, balanced carrier transport, and minimized parasitic capacitance, the device achieves a 3-dB bandwidth of 206 GHz and an external responsivity of 0.8 A/W, setting a new benchmark for BEP. Packaged with WR-5.1 waveguide output, it delivers radio-frequency (RF) power exceeding -5 dBm across the 127–185 GHz frequency range. As a proof of concept, we achieved a wireless transmission of 54 meters with a single-line rate of up to 120 Gbps, leveraging photonics-aided technology without requiring a low-noise amplifier (LNA). This work establishes a pathway to significantly enhance optical power budgets and reduce energy consumption, presenting a transformative step toward high-bandwidth, high-efficiency sub-THz communication systems and next-generation wireless networks.**

## Introduction

Driven by emerging real-time services like telemedicine, autonomous driving, and virtual reality<sup>1,2</sup>, the surge in wireless communication traffic has saturated traditional microwave frequency bands, prompting a shift towards the sub-terahertz (sub-THz) spectrum<sup>3,4</sup>. Photonic-assisted THz technologies have emerged as a compelling alternative to all-electronic methods, offering unparalleled advantages such as broad frequency bandwidth, tunability, and intrinsic stability<sup>5</sup>. These attributes make photonic approaches particularly suited to addressing the high-capacity demands of future communication systems. At the heart of photonic THz-wave generation are ultra-fast photodiodes (PDs), which serve as the critical interface for optical-to-electrical conversion through photo-mixing. The performance of these devices dictates the system's maximum operating frequency, dynamic range, and overall efficiency, making their development pivotal to advancing THz communication technologies<sup>6,7</sup>.

However, existing high-speed PDs face limitations in photoelectric conversion efficiency near the sub-THz range, creating a dependency on high input optical power and post-amplification before transmission<sup>8,9</sup>. This dependence can increase energy con-

sumption and risk nonlinear distortions in practical use. To overcome these challenges, PDs must achieve high saturation power, high responsivity, and wide bandwidth concurrently to enhance the performance and efficiency of sub-THz systems.

Among various types of ultra-fast photodiode, the uni-traveling-carrier photodiode (UTC-PD) has exhibited the highest output power in sub-THz regime, with continuous structural modifications since its introduction in 1997<sup>10</sup>. These pioneering works effectively address the carrier screening issue<sup>11</sup> by utilizing the fast electrons from the InP platform as active carriers in the collector<sup>12,13</sup>. Surface-illuminated modified UTC-PDs (MUTC-PDs) have demonstrated the ability to achieve THz-level bandwidths of 100-330 GHz (refs.<sup>14-18</sup>) and high output power by thinning the absorber, reducing PD sizes and incorporating inductance peaking. However, this miniaturization leads to reduced optical absorption and considerable coupling losses, consequently decreasing efficiency and responsivities.

In contrast, waveguide photodiodes (WG-PDs) offer a promising solution to the inherent trade-off between efficiency and speed by laterally coupling light into the active region through an optical waveguide<sup>19-21</sup>. Recent advancements report a record 3-dB bandwidth exceeding 220 GHz and a responsivity of 0.24 A/W for InP-based evanescently coupled waveguide MUTC-PDs, with high saturation power reaching -1.69 dBm at 215 GHz due to the uniform light distribution<sup>21</sup>. For sub-THz speed, comprehensive engineering of carrier transport and RC response is needed. However, reducing the PD size to below 30 μm<sup>20,21</sup>—typically preferred for better RC response—introduces challenges in achieving efficient coupling due to the corresponding reduction in the absorption length. This trade-off between efficiency and RC time constant has led to previously reported ultra-fast WG-PDs facing a persistent 55 GHz × 100% bottleneck<sup>22</sup> in bandwidth-efficiency product (BEP). Therefore, developing a UTC-PD with an enhanced BEP, higher speed, and the ability to serve as a photonic sub-THz source with low power consumption, compact design, and wide bandwidth remains a critical and sought-after goal.

In this work, we demonstrate waveguide-integrated MUTC-PDs with a record-breaking BEP exceeding 130 GHz × 100%, effectively doubling the highest BEP reported to date<sup>22</sup>. This outstanding performance is achieved through several synergistic strategies: fine-tuning the electric field distribution, balancing carrier transport, and incorporating benzocyclobutene (BCB) beneath the electrodes to minimize parasitic capacitance, while simultaneously integrating a spot-size converter (SSC) to enhance external responsivity and overall device efficiency. Our design achieves an unprecedented 3-dB bandwidth of 270 GHz for 2 × 7 μm<sup>2</sup> PDs, the highest reported among all III-V WG-PDs. Meanwhile, the 2 × 15 μm<sup>2</sup> devices set a new BEP record of 131.9 GHz × 100%, with bandwidths exceeding 200 GHz and an external responsivity of 0.8 A/W. To showcase the device's capability in data transmission



between 127 GHz and 185 GHz, with power maintained above -10 dBm across the entire G-band. Furthermore, leveraging photonics-aided technology and eliminating the need for a low-noise amplifier (LNA), we successfully achieved a 54-meter wireless link at data rates up to 120 Gbps, highlighting the device's exceptional capabilities for next-generation, high-capacity wireless networks.

## Results

### Device structure and design

Fig. 1a shows the concept and structure of the proposed waveguide-integrated PD chip, which includes an SSC, a MUTC-PD structure and a coplanar waveguide (CPW). Fig. 1b shows the corresponding scanning electron microscope (SEM) image. The 2-step SSC is utilized to achieve efficient optical coupling within compact coupling length, ensuring both high responsivity and fast RC response simultaneously. The first section is a 1.5- $\mu\text{m}$ -thick diluted waveguide, designed to facilitate fiber-to-waveguide coupling through mode field matching<sup>23,24</sup>. For an input Gaussian beam with a 2- $\mu\text{m}$  diameter spot size, this structure achieves a simulated coupling loss as low as 0.2 dB. The second section consists of two InGaAsP optical matching layers, which provide a gradual increase of the optical refractive index from the diluted waveguide to the PD's active region, thereby enhancing upward light guidance into the active area as small as 30  $\mu\text{m}^2$ . The external responsivity of the 2  $\times$  15  $\mu\text{m}^2$  device was simulated with respect to different matching layer thickness, with SiO<sub>2</sub> on the waveguide facet serving as the anti-reflection coating, as shown in Fig. 1f. The optimal responsivity of 0.83 A/W is obtained when the thickness of the first matching layer (Q1.03) and the second matching (Q1.33) layer is 210 nm and 320 nm respectively. Fig. 1g shows the simulated optical intensity as light propagates through the device.

The cross section of the MUTC structure is shown in Fig. 1c, which contains a P-doped partially depleted InGaAs absorption layer (165 nm) positioned between an InP diffusion block layer and an InP drift layer. A 30 nm cliff layer with doping level of 2  $\times$  10<sup>17</sup> cm<sup>-3</sup> is inserted in the drift layer to enable rapid electron transport by precisely shaping the electric field. Fig. 1d shows the simulated electric field distribution for the 2  $\times$  15  $\mu\text{m}^2$  device at various photocurrent levels. The heavily doped cliff layer effectively boosts the electric field across the InGaAs/InP interfaces (blue region), aiding electron movement across the heterogeneous inter-facial barrier and thereby alleviating the current blocking effect<sup>25</sup>. It also maintains an electric field of 20-50 kV/cm throughout the entire e-drift layer (grey region) at photocurrent up to 10 mA, facilitating electron overshoot<sup>26</sup> and ensuring a short electron transit time. Additionally, this electric field regulation helps counteract space charge effects at high currents, leading to improved high-power performance. To further reduce the carrier transit time, the depleted absorber is designed to be 100 nm thick, which is noticeably thicker than the 30 nm thickness typically used in the reported MUTC-PDs with ultra-wide bandwidth<sup>17,18,27</sup>. This design effectively reduces the proportion of diffusion current from the p-type absorber, thereby allowing more electrons to be transported efficiently with the high electric field in the depletion region. Fig. 1e illustrates the calculated transit-limited bandwidth as the thickness of the depleted absorber ( $W_d$ ) varies from 50 to 150 nm. The bandwidth initially increases significantly due to the reduced electron diffusion time. When  $W_d$  exceeds 100 nm, the increased contribution of slower-responding hole currents in the depleted absorption region starts to slow down the overall transit process. Consequently, a thickness of 100 nm is chosen to balance the response of electrons and hole currents, leading to an optimal transit-limited bandwidth of 413 GHz. Moreover, thicker  $W_d$  also

helps small-size devices maintain acceptable junction capacitance.

Apart from transit time and junction capacitance, parasitic parameters are another critical factor affecting bandwidth. To address this, the introduction of a low dielectric constant material, such as BCB, beneath the CPW structure can effectively reduce the electrode parasitic capacitance<sup>21</sup>, thereby enhancing the RC-time-limited bandwidth. As shown in Fig. 1h (table format) and Fig. 1i, the 3-dB bandwidth of the 2  $\times$  15  $\mu\text{m}^2$  device, accounting for both RC and transit frequency responses, was meticulously simulated for various BCB thicknesses. Notably, the implementation of 1  $\mu\text{m}$  thick BCB significantly enhanced the 3-dB bandwidth by approximately 30 GHz compared with the traditional scheme, where CPW electrodes are deposited directly on the InP substrate. As the BCB thickness increased to 5  $\mu\text{m}$ , the device achieved a 3-dB bandwidth of 205 GHz, with only marginal improvements observed with further increases in thickness. Considering both the bandwidth enhancement and fabrication feasibility, the BCB thickness was ultimately controlled within the range of 5 to 8  $\mu\text{m}$ . The complete simulation process, utilizing "field-circuit co-simulation", is provided in Supplementary Note 2.

### Characterization of PDs

The dark current characteristics for devices with varying lengths are depicted in Fig. 2a. A typical dark current is observed to be around 200 pA at a -2 V bias. In Fig. 2b, both the measured and simulated external responsivities for devices with different lengths are shown. Devices with lengths of 7  $\mu\text{m}$ , 10  $\mu\text{m}$ , and 15  $\mu\text{m}$  exhibit external responsivities of 0.28 A/W, 0.52 A/W, and 0.8 A/W, respectively, at a wavelength of 1550 nm. The simulated external responsivity as a function of PD length, calculated using Ansys Lumerical FDTD, is represented by the solid line, which demonstrates strong agreement with the experimental results.

In Fig. 2c-e, the frequency response of devices with lengths of 7  $\mu\text{m}$ , 10  $\mu\text{m}$ , and 15  $\mu\text{m}$  is depicted at a -1 V bias voltage, corresponding to photocurrents of 1.5 mA, 2.2 mA, and 3 mA, respectively. The 2  $\times$  7  $\mu\text{m}^2$  device exhibits an ultra-wide bandwidth of 270 GHz, showcasing the highest performance in terms of speed among waveguide-type PDs. The 2  $\times$  10  $\mu\text{m}^2$  and 2  $\times$  15  $\mu\text{m}^2$  devices, with larger active areas, show bandwidth of 250 GHz and 206 GHz, respectively. The reduction in bandwidth is attributed to the growing junction capacitance, indicating that the RC time constant is the major limiting factor. Nonetheless, thanks to effective parasitic capacitance optimization, the largest device still maintains a bandwidth exceeding 200 GHz and achieves a record-high BEP of 131.9 GHz.

The saturation performance of PDs is assessed by measuring the RF output power as a function of the average photocurrent near their cutoff frequency. Fig. 2f,g illustrate the output power for devices with lengths of 7  $\mu\text{m}$  and 10  $\mu\text{m}$  under different voltages. Increasing the bias voltage mitigates carrier accumulation by enhancing the electric field, thereby increasing the saturation current. Both the 2  $\times$  7  $\mu\text{m}^2$  and 2  $\times$  10  $\mu\text{m}^2$  devices exhibit optimal performance at -1.5 V bias, with the highest output powers of -9.0 dBm at 280 GHz and -5.9 dBm at 250 GHz, respectively. For biases above 1.5 V, the increased thermal effect and excessive electric fields in the drift region slow down electron transport, which in turn reduces the output power. The frequency-dependent saturation performance of the 2  $\times$  15  $\mu\text{m}^2$  device, measured at -1.5 V bias, is shown in Fig. 2h. The 15  $\mu\text{m}$  coupling length ensures a more uniform light intensity distribution, achieving a saturation photocurrent of around 9 mA across various frequencies. The device delivers high output powers of 0.4 dBm at 160 GHz and -2.4 dBm at 220 GHz, respectively. However, due to RC limitations, the saturation power drops by approximately 7 dB from

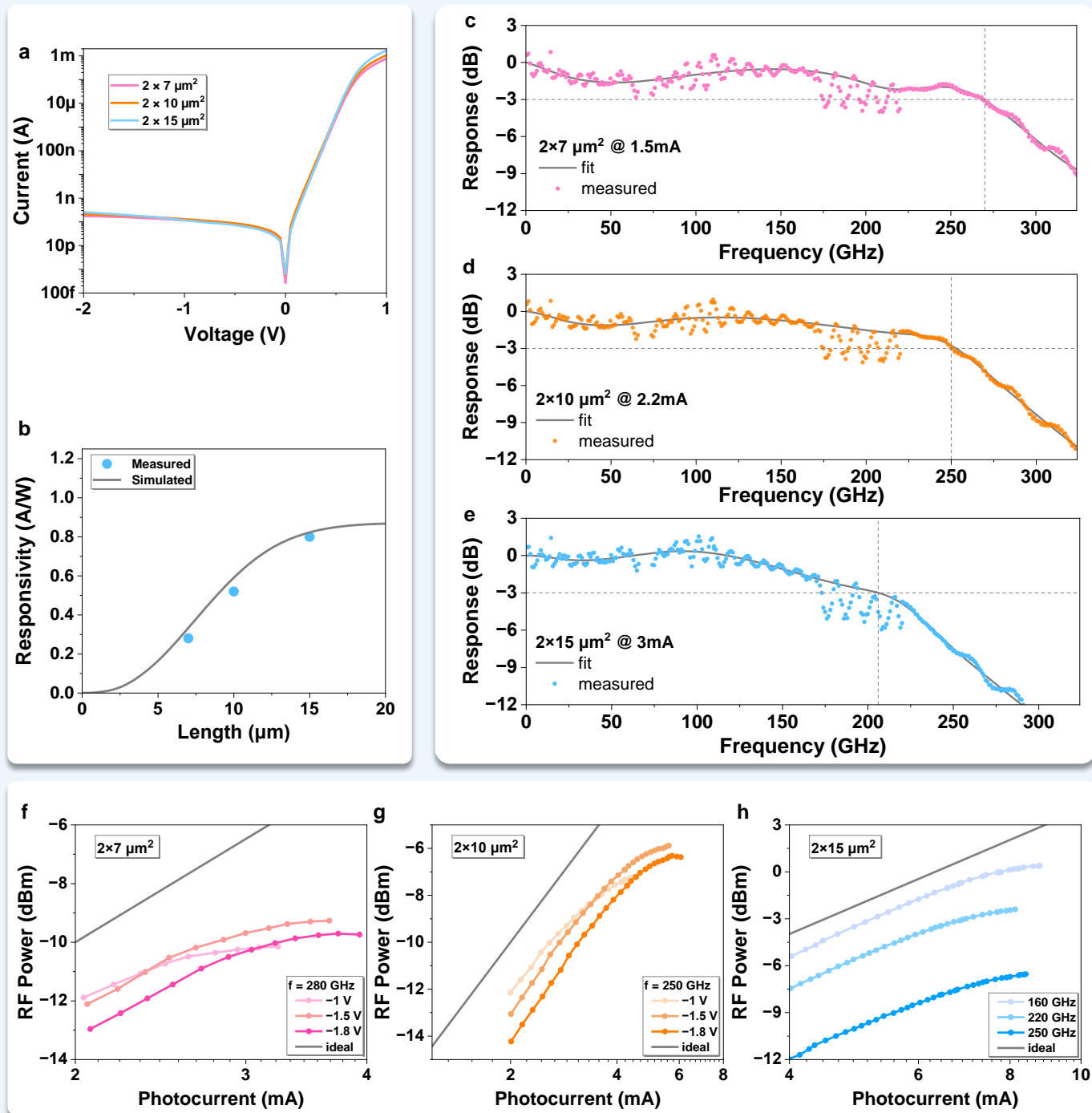


**Figure 2: Measured static and dynamic performance of PDs.** **a**, Dark current versus bias voltage characteristic for the devices with different lengths. **b**, Measured external (blue dots) responsivities and simulated external responsivities (solid line) of the devices with different lengths. **c-e**, Frequency response from a heterodyne measurement set-up of the  $2 \times 7 \mu\text{m}^2$  device (**c**) at 1.5 mA photocurrent,  $2 \times 10 \mu\text{m}^2$  device (**d**) at 2.2 mA photocurrent and  $2 \times 15 \mu\text{m}^2$  device (**e**) at 3 mA photocurrent under -1 V bias. Dots are measured data, and the grey line is the polynomial fit. The corresponding 3-dB bandwidths reach 270 GHz, 250 GHz and 206 GHz, respectively. **f**, **g**, RF power versus photocurrent for the  $2 \times 7 \mu\text{m}^2$  device (**f**) at 280 GHz and  $2 \times 10 \mu\text{m}^2$  device (**g**) at 250 GHz, measured from -1 V to -1.8 V. **h**, RF power versus photocurrent for the  $2 \times 15 \mu\text{m}^2$  device at frequencies of 160 GHz, 220 GHz and 250 GHz, measured at -1.5 V bias.

160 GHz to 250 GHz. With its high responsivity and substantial output power up to 220 GHz, the  $2 \times 15 \mu\text{m}^2$  device is particularly well-suited for G-band THz communication applications.

#### Packaged module and THz wireless communication

As the operating frequency exceeds 100 GHz, PDs packaged with coaxial connectors face challenges in achieving low-loss output, primarily due to dielectric losses, higher-order modes, and elec-

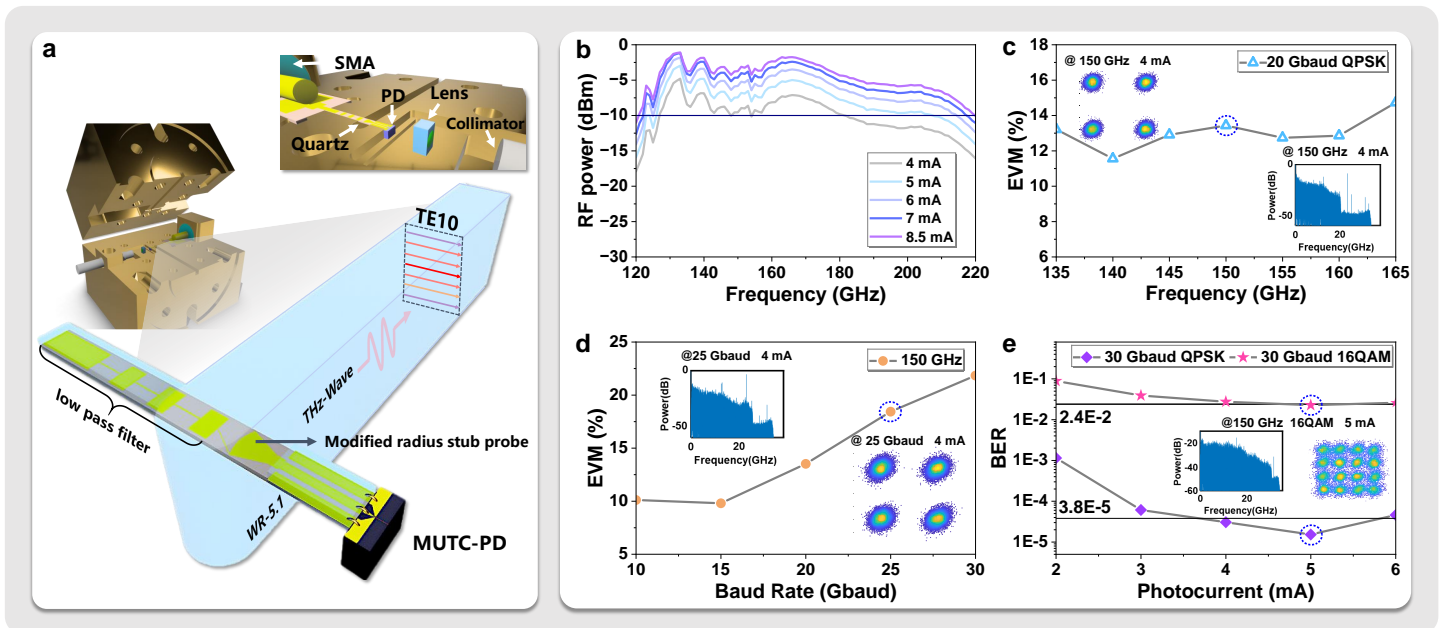


**Figure 3: WR-5.1 waveguide packaged MUTC-PD module and the results of photonics-aided sub-THz communication without THz amplifier.** **a**, Schematic of the WR-5.1 waveguide packaged MUTC-PD module. **b**, Frequency response of the packaged module under different photocurrents from 120 GHz to 220 GHz. **c**, EVM as a function of transmission frequency for a 20 Gbaud QPSK signal at a photocurrent of 4 mA. **d**, EVM versus baud rate for a 150 GHz carrier signal at a photocurrent of 4 mA. **e**, BER versus photocurrent for 30 Gbaud QPSK/16-QAM signal at a carrier frequency of 150 GHz.

tromagnetic interference. In contrast, waveguides provide low-loss output over a wide frequency range<sup>28–31</sup>, while also enabling seamless integration with other standard waveguide interface devices, such as antennas, amplifiers, and mixers.

To meet the demand for high-efficiency sub-THz wireless communication systems, we have designed a WR-5.1 waveguide packaged module, as illustrated in Fig. 3a. In this design, light is coupled into the SSC using a cost-effective solution that includes a single-mode fiber, collimator, and microlens. The PD electrodes are connected to a 50  $\mu\text{m}$  thick quartz passive circuit via wire bonding, which integrates a transition from the CPW to a modified radius stub probe to facilitate low-loss transmission of RF signals. It also enables the excitation of the TE<sub>10</sub> mode in the rectangular waveguide. A step-impedance low-pass filter is incorporated to prevent RF signal leakage while providing a DC bias to the PD. Through careful design and optimization of the quartz passive circuit, we achieve an insertion loss of approximately 0.5 dB across the frequency range of 140–220 GHz, ensuring minimal RF loss. A back-to-back module is employed to characterize the loss properties, with detailed descriptions provided in Supplementary Note 4.

After packaging the  $2 \times 15 \mu\text{m}^2$  device without an anti-reflective (AR) coating, the responsivity of the module is measured to be 0.5 A/W. The frequency response of the packaged module under different photocurrents is shown in Fig. 3b. At a photocurrent of 8.5 mA, the output power exceeds -5 dBm from 127 GHz to 185 GHz, and remains above -10 dBm across the entire G-band. These results demonstrate the substantial potential of the MUTC-PD module for applications in short-range radar, indoor communication, long-range (hundred-meter) transmission, and other related scenarios.

Fig. 3c-e present experimental results of photonics-aided sub-THz wireless transmission over 54 m using the waveguide-packaged MUTC-PD module. The experimental setup is described in detail in Supplementary Note 5. Fig. 3c shows the error

vector magnitude (EVM) curve for a 20 Gbaud quadrature phase shift keying (QPSK) signal transmitted over 54 meters in the 135 GHz to 165 GHz frequency range. The EVM remains below 15%, well below the 17.5% threshold for QPSK signals, indicating that the module provides sufficient saturated output power for 54-meter wireless transmission without the need for THz amplification. Fig. 3d shows the relationship between EVM and baud rate for the QPSK signal. At a photocurrent of 4 mA, the module supports the generation and transmission of a 30 Gbaud QPSK signal over 54 meters. Although the module can support a wider bandwidth, the mixer used in the experimental setup limits the achievable transmission rate, preventing higher rates from being demonstrated. The 25 Gbaud QPSK constellation diagram in Fig. 3d shows near-error-free transmission. Further transmission experiments are conducted with 30 Gbaud QPSK and 16-quadrature amplitude modulation (QAM) signals, centered at 150 GHz. Fig. 3e shows the bit error rate (BER) as a function of photocurrent after 54 meters of wireless transmission. As photocurrent increases, the RF signal power also increases, resulting in a reduction in BER. At a photocurrent of 5 mA, the BERs for 30 Gbaud QPSK and 16-QAM signals are  $3 \times 10^{-5}$  and  $2.3 \times 10^{-2}$ , respectively—both well below the hard-decision forward error correction (FEC) ( $3.8 \times 10^{-5}$ ) and soft-decision FEC ( $2.4 \times 10^{-2}$ ) thresholds. These results demonstrate that the transmission system can support a line rate of 120 Gbps over 54 m without THz amplifiers, highlighting the substantial improvements in output power and efficiency achieved with the designed MUTC-PD module.

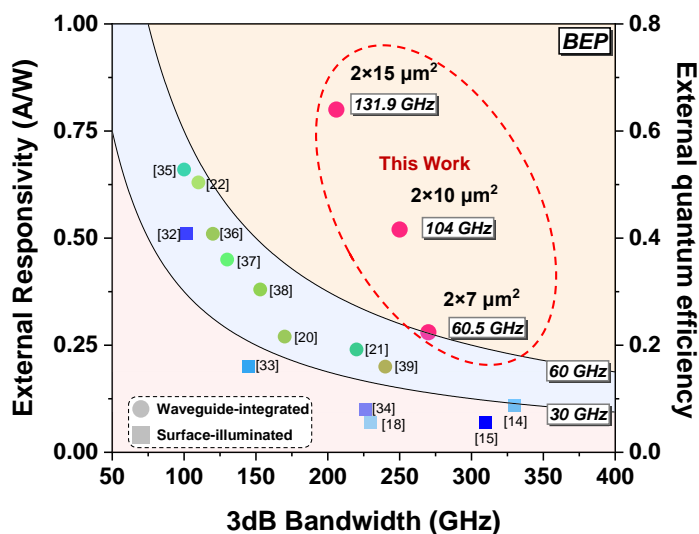
## Discussion

Fig. 4 provides an overview of state-of-the-art waveguide-coupled and surface illuminated PDs, with detailed parameters summarized in Supplementary Note 6. While surface-illuminated PDs have demonstrated impressive speed performance, reaching up to 330 GHz, their responsivity significantly decreases as the bandwidth increases, particularly for PDs with bandwidths exceeding

**Table I: Comparison of short-distance photonics-aided transmission systems**

Year/reference	PD type	Frequency (GHz)	LNA gain (dB)	Bit Rate (Gbps)	Distance (m)
2022 <sup>40</sup>	UTC-PD	135	0	60	3
2022 <sup>41</sup>	UTC-PD	130	0	60	BTB
2022 <sup>42</sup>	UTC-PD	120	30	55	200
2023 <sup>43</sup>	UTC-PD	112	30	57.2	13
2024 <sup>44</sup>	UTC-PD	120	30	72	70
2024 <sup>45</sup>	MUTC-PD	150	18	75	1
2024 <sup>46</sup>	MUTC-PD	131	18	120	1
This work	MUTC-PD	150	<b>0</b>	<b>120</b>	<b>54</b>

LNA, low noise amplifier; BTB, back to back.



**Figure 4: The performance comparison of waveguide-coupled and surface illuminated PDs.** 3dB bandwidths and external responsivities of waveguide coupled and surface-illuminated PDs reported in literature<sup>14,15,18,20–22,32–39</sup>.

200 GHz. WG-PDs, on the other hand, decouple the optical coupling direction from the carrier transport path, enabling BEP between 37 and 55 GHz  $\times$  100% by realizing both efficient absorption and short carrier transit times. In this work, the  $2 \times 15 \mu\text{m}^2$  device demonstrates an enhanced bandwidth of 206 GHz and an external responsivity of 0.8 A/W, resulting in a breakthrough BEP of 131.9 GHz  $\times$  100%. Additionally, the  $2 \times 7 \mu\text{m}^2$  device achieves a record bandwidth of 270 GHz among all waveguide-coupled PDs. This exceptional performance can be attributed to the integration of a SSC, optimization of carrier transport, and the reduction of parasitic capacitance.

Table 1 summarizes the latest progress in short-distance photonics-aided transmission systems within the 110 GHz to 170 GHz frequency range, detailing parameters such as center frequency, PD type, LNA gain, transmission rate, and distance. Here, an LNA gain of 0 dB indicates that no THz amplifier was used in the transmission system. As shown in Table 1, previously reported systems without an LNA can only achieve bit rates of up to 60 Gbps with a short transmission distance of 3 meters, limiting their practical applications. While the inclusion of an LNA improves both the transmission rate and distance, it comes at the cost of higher energy consumption and risk of nonlinear distortions. In contrast, we experimentally demonstrate a single-line rate of 120 Gbps over a 54-meter transmission distance without the use

of THz amplifiers. At a bias voltage of -1.5 V and a photocurrent of 5 mA, the corresponding RF power and efficiency of our MUTC-PD module are sufficient to support wireless transmission over 54 meters, achieving an improved data rate.

In conclusion, we have demonstrated a waveguide-integrated MUTC-PD with an ultra-high bandwidth exceeding 200 GHz and a record BEP of 131.9 GHz. After packaged with a WR-5.1 waveguide output, the device can support 54-meter wireless transmission at a single line rate of up to 120 Gbps, utilizing photonics-aided technology without any LNA. This work emphasizes the potential of InP photonics integrated circuits for efficient THz generation, paving the way for next-generation wireless communication systems with enhanced optical power budgets.

## Methods

### Device fabrication

The epitaxial structure of the designed MUTC-PD was grown by a metal-organic chemical vapor deposition (MOCVD) system on a 2-inch semi-insulating InP substrate. The device was fabricated into a triple-mesa structure. Inductively coupled plasma (ICP) dry etching process was conducted to achieve vertical sidewalls and precise control of mesa dimensions, while wet etching ( $\text{H}_3\text{PO}_4:\text{HCl} = 1:3$ ) was used for electrical isolation between n-mesas. Following the etching steps, Ti/Pt/Au/Ti and GeAu/Ni/Au layers were deposited to form the p-contact and n-contact, respectively, with a rapid thermal annealing process conducted at 360 °C. After passivating the sidewalls with a BCB layer, Ti/Au layers were deposited to create CPW pads. Detailed fabrication process flow can be found in the Supplementary Note 1.

### DC electrical measurements

The dark current was measured with Keysight B1500 semiconductor parameter analyzer at room temperature. The responsivity of the device was characterized with a laser source (Keysight 81606A) and a source measurement unit (SMU, Keysight B2901A). Light from a cleaved single-mode fiber was coupled to the waveguide through an automated fiber alignment process. Polarization was manually optimized using a polarization controller. The laser wavelength was set to 1550 nm, and the power at the fiber tip was measured using an optical power meter (Thorlabs PM400). External responsivity was calculated as the ratio of the photocurrent to the optical power at the fiber tip, under the desired voltage.

### RF measurements

The frequency response and the saturation performance of the InGaAs/InP waveguide devices and packaged module were inves-

tigated by an optical heterodyne setup. Two tunable lasers with wavelengths near 1.55  $\mu\text{m}$  were combined to generate a heterodyne beat note with a wide frequency tuning range from Megahertz to Terahertz.

For PD chips, the output RF power was obtained by two measurement setups. From DC to 110 GHz, the RF signal was collected by the Rohde & Schwarz power meter (NRP2) through the GSG Model 110H probe. Frequency-dependent loss value introduced by cables, bias tee and GSG probe was calibrated by a vector network analyzer (VNA) with corresponding calibration kit (85058E & CS-5 for DC to 67 GHz, WR10-VDI & CS-5 for 73.8 GHz to 110 GHz). As frequencies exceed 110 GHz, a VDI power meter (PM5) and a set of waveguide probes covering 110 GHz to 325 GHz were used to measure the THz power generation. The loss of the probes and waveguide tapers provided by the manufacturer was de-embedded from the measurement results. Similarly, since the packaged module featured a standard waveguide interface, the output RF power can be easily obtained by a matched waveguide taper and VDI power meter (PM5). The detailed schematics of two measurement setups can be founded in Supplementary Note 3.

## Data availability

The data that support the findings of this study are available from the figures and from the corresponding authors on reasonable request.

## Acknowledgments

The PD chips were fabricated with support from the ShanghaiTech Material and Device Lab (SMDL).

## Author contributions

B.Chen conceived the idea. L. Li, Z. Zhang, and B.Chen designed the device epi-layer structure. L. Li, T. Long, L. Wang, Z. Zhang, and J. Wang jointly fabricated the devices and participated in the testing process. T. Long designed and packaged the WR-5.1 module and tested its performance. J. Yu, X. Yang, T. Long, M. Wang, and Z. Zhang conducted the terahertz communication experiment. L. Li, T. Long, X. Yang, J. Wang, M. Wang, J. Yu, J. Lu, and B.Chen primarily wrote the manuscript. B.Chen and J. Yu supervised the research.

## Competing interests

The authors declare no competing interests.

\* These authors contributed equally to this work.

† [jianjun@fudan.edu.cn](mailto:jianjun@fudan.edu.cn)

‡ [chenbl@shanghaitech.edu.cn](mailto:chenbl@shanghaitech.edu.cn)

<sup>1</sup> T. Nagatsuma, G. Ducourmau, and C. C. Renaud, *Nature Photonics* **10**, 371 (2016).

<sup>2</sup> M. Sung, S.-R. Moon, E.-S. Kim, S. Cho, J. K. Lee, S.-H. Cho, T. Kawanishi, and H.-J. Song, *IEEE Wireless Communications* **28**, 185 (2021).

<sup>3</sup> H. Zhang, L. Zhang, S. Wang, Z. Lu, Z. Yang, S. Liu, M. Qiao, Y. He, X. Pang, X. Zhang, *et al.*, *Journal of Lightwave Technology* **39**, 5783 (2021).

<sup>4</sup> G. Kang, Y. Lee, J. Kim, D. Yang, H. K. Nam, S. Kim, S. Baek, H. Yoon, J. Lee, T.-T. Kim, *et al.*, *Nanophotonics* **13**, 983 (2024).

<sup>5</sup> L. Zhang, X. Pang, S. Jia, S. Wang, and X. Yu, *IEEE Communications Magazine* **58**, 34 (2020).

<sup>6</sup> J. P. Seddon, M. Natrella, X. Lin, C. Graham, C. C. Renaud, and A. J. Seeds, *IEEE Journal of Selected Topics in Quantum Electronics* **28**, 1 (2022).

<sup>7</sup> T. Ishibashi, Y. Muramoto, T. Yoshimatsu, and H. Ito, *IEEE Journal of Selected Topics in Quantum Electronics* **20**, 79 (2014).

<sup>8</sup> S. Ummethala, T. Harter, K. Koehnle, Z. Li, S. Muehlbrandt, Y. Kutuvantavida, J. Kemal, P. Marin-Palomo, J. Schaefer, A. Tessmann, *et al.*, *Nature photonics* **13**, 519 (2019).

<sup>9</sup> M. Zhu, J. Zhang, B. Hua, M. Lei, Y. Cai, L. Tian, D. Wang, W. Xu, C. Zhang, Y. Huang, *et al.*, *Science China Information Sciences* **66**, 113301 (2023).

<sup>10</sup> T. Ishibashi, N. Shimizu, S. Kodama, H. Ito, T. Nagatsuma, and T. Furuta, in *Ultrafast Electronics and Optoelectronics* (Optica Publishing Group, 1997) p. UC3.

<sup>11</sup> T. Ishibashi and H. Ito, *Journal of Applied Physics* **127** (2020).

<sup>12</sup> T. Ishibashi and H. Ito, *IEEE Journal of Selected Topics in Quantum Electronics* **28**, 1 (2022).

<sup>13</sup> T. Ishibashi, T. Furuta, H. Fushimi, S. Kodama, H. Ito, T. Nagatsuma, N. Shimizu, and Y. Miyamoto, *IEICE transactions on electronics* **83**, 938 (2000).

<sup>14</sup> J.-M. Wun, Y.-W. Wang, and J.-W. Shi, *IEEE Journal of Selected Topics in Quantum Electronics* **24**, 1 (2018).

<sup>15</sup> H. Ito, T. Furuta, S. Kodama, and T. Ishibashi, *Electronics Letters* **36**, 1 (2000).

<sup>16</sup> Y.-C. Huang, N.-W. Chen, Y.-K. Wu, Naseem, and J.-W. Shi, *Journal of Lightwave Technology* **42**, 2362 (2024).

<sup>17</sup> C. Wei, X. Xie, Z. Wang, Y. Chen, Z. Zeng, X. Zou, W. Pan, and L. Yan, *Journal of Lightwave Technology* **41**, 7238 (2023).

<sup>18</sup> Y. Tian, B. Xiong, C. Sun, Z. Hao, J. Wang, L. Wang, Y. Han, H. Li, L. Gan, and Y. Luo, *Opt. Express* **31**, 23790 (2023).

<sup>19</sup> Q. Li, K. Sun, K. Li, Q. Yu, P. Runge, W. Ebert, A. Beling, and J. C. Campbell, *Journal of Lightwave Technology* **35**, 4752 (2017).

<sup>20</sup> E. Rouvalis, M. Chtioui, F. van Dijk, F. Lelarge, M. J. Fice, C. C. Renaud, G. Carpintero, and A. J. Seeds, *Opt. Express* **20**, 20090 (2012).

<sup>21</sup> L. Li, L. Wang, T. Long, Z. Zhang, J. Lu, and B. Chen, *Journal of Lightwave Technology* **42**, 7451 (2024).

<sup>22</sup> K. Kato, A. Kozen, Y. Muramoto, Y. Itaya, T. Nagatsuma, and M. Yaita, *IEEE Photonics Technology Letters* **6**, 719 (1994).

<sup>23</sup> P. Runge, F. Ganzer, J. Gläsel, S. Wünsch, S. Mutschall, and M. Schell, in *2020 Optical Fiber Communications Conference and Exhibition (OFC)* (2020) pp. 1–3.

<sup>24</sup> S. Demiguel, N. Li, X. Li, X. Zheng, J. Kim, J. Campbell, H. Lu, and A. Anselm, *IEEE Photonics Technology Letters* **15**, 1761 (2003).

<sup>25</sup> Z. Li, H. Pan, H. Chen, A. Beling, and J. C. Campbell, *IEEE Journal of Quantum Electronics* **46**, 626 (2010).

<sup>26</sup> T. Maloney and J. Frey, *Polar* **12**, 0 (1977).

<sup>27</sup> Q. Li, K. Li, Y. Fu, X. Xie, Z. Yang, A. Beling, and J. C. Campbell, *Journal of Lightwave Technology* **34**, 2139 (2016).

<sup>28</sup> H. Ito, T. Ito, Y. Muramoto, T. Furuta, and T. Ishibashi, *Journal of lightwave technology* **21**, 3456 (2003).

<sup>29</sup> T. Furuta, T. Ito, Y. Muramoto, H. Ito, M. Tokumitsu, and T. Ishibashi, *Electronics Letters* **41**, 1 (2005).

<sup>30</sup> H. Ito, T. Furuta, Y. Muramoto, T. Ito, and T. Ishibashi, *Electronics Letters* **42**, 1424 (2006).

<sup>31</sup> T. Kurokawa, T. Ishibashi, M. Shimizu, K. Kato, and T. Nagatsuma, *Electronics Letters* **54**, 705 (2018).

<sup>32</sup> B. Xiong, Y. Tian, C. Sun, Z. Hao, J. Wang, L. Wang, Y. Han, H. Li, L. Gan, and Y. Luo, in *2024 Optical Fiber Communications Conference and Exhibition (OFC)* (2024) pp. 1–3.

<sup>33</sup> A. Beling, T. C. Tzu, J. Gao, J. S. Morgan, K. Sun, N. Ye, B. Tossoun, F. Yu, and Q. Yu, in *2019 24th OptoElectronics and Communications Conference (OECC) and 2019 International Conference on Photonics in Switching and Computing (PSC)* (2019) pp. 1–3.

<sup>34</sup> T. Umezawa, P. T. Dat, Y. Yoshida, S. Nakajima, A. Matsumoto, K. Akahane, A. Kanno, and N. Yamamoto, in *2024 Optical Fiber Communications Conference and Exhibition (OFC)* (2024) pp. 1–3.

<sup>35</sup> H.-G. Bach, A. Beling, G. Mekonnen, R. Kunkel, D. Schmidt,

- W. Ebert, A. Seeger, M. Stollberg, and W. Schlaak, *IEEE Journal of Selected Topics in Quantum Electronics* **10**, 668 (2004).
- <sup>36</sup> A. Beling, H.-G. Bach, G. Mekonnen, R. Kunkel, and D. Schmidt, *IEEE Photonics Technology Letters* **17**, 2152 (2005).
- <sup>37</sup> P. Runge, G. Zhou, F. Ganzer, S. Mutschall, and A. Seeger, in *2015 European Conference on Optical Communication (ECOC)* (2015) pp. 1–3.
- <sup>38</sup> M. Sun, B. Xiong, C. Sun, Z. Hao, J. Wang, L. Wang, Y. Han, H. Li, L. Gan, and Y. Luo, *Opt. Express* **32**, 16455 (2024).
- <sup>39</sup> S. Lischke, A. Peczek, J. Morgan, K. Sun, D. Steckler, Y. Yamamoto, F. Korndörfer, C. Mai, S. Marschmeyer, M. Fräschke, *et al.*, *Nature Photonics* **15**, 925 (2021).
- <sup>40</sup> W. Zhou, L. Zhao, J. Zhang, K. Wang, J. Yu, Y.-W. Chen, S. Shen, R.-K. Shiu, and G.-K. Chang, *Journal of Lightwave Technology* **38**, 3592 (2020).
- <sup>41</sup> P. T. Dat, K. Inagaki, A. Kanno, and K. Akahane, in *2022 RIVF International Conference on Computing and Communication Technologies (RIVF)* (IEEE, 2022) pp. 1–5.
- <sup>42</sup> K. Wang, C. Wang, W. Li, Y. Wang, J. Ding, C. Liu, M. Kong, F. Wang, W. Zhou, F. Zhao, *et al.*, *Journal of Lightwave Technology* **40**, 2791 (2022).
- <sup>43</sup> L. Zhao, K. Wang, and W. Zhou, *Optics Express* **31**, 2270 (2023).
- <sup>44</sup> Q. Chen, W. You, K. Liu, S. Wang, L. Zhao, and H. Wen, *Optical Fiber Technology* **87**, 103925 (2024).
- <sup>45</sup> Y. Tian, B. Dong, Y. Li, B. Xiong, J. Zhang, C. Sun, Z. Hao, J. Wang, L. Wang, Y. Han, *et al.*, *Opto-Electronic Science* **3**, 230051 (2024).
- <sup>46</sup> Y. Tian, Y. Li, B. Dong, B. Xiong, J. Zhang, C. Sun, Z. Hao, J. Wang, L. Wang, Y. Han, *et al.*, *Journal of Lightwave Technology* (2024).